Published in final edited form as:
Ultrasound Med Biol. 2009 February ; 35(2): 278–295. doi:10.1016/j.ultrasmedbio.2008.08.015.

ARFI Imaging for Noninvasive Material Characterization of Atherosclerosis Part II: Toward In Vivo Characterization

Russell H. Behler[1], **Timothy C. Nichols**[2], **Hongtu Zhu**[3], **Elizabeth P. Merricks**[2], and **Caterina M. Gallippi**[1]

[1]Joint Department of Biomedical Engineering, University of North Carolina at Chapel Hill and North Carolina State University, Chapel Hill NC, USA

[2]Department of Pathology and Laboratory Medicine, University of North Carolina at Chapel Hill, Chapel Hill NC, USA

[3]Department of Biostatistics, University of North Carolina at Chapel Hill, Chapel Hill NC, USA

Abstract

Seventy percent of cardiovascular disease (CVD) deaths are attributed to atherosclerosis. Despite their clinical significance, nonstenotic atherosclerotic plaques are not effectively detected by conventional atherosclerosis imaging methods. Moreover, conventional imaging methods are insufficient for describing plaque composition, which is relevant to cardiovascular risk assessment. Atherosclerosis imaging technologies capable of improving plaque detection and stratifying cardiovascular risk are needed. Acoustic Radiation Force Impulse (ARFI) ultrasound, a novel imaging method for noninvasively differentiating the mechanical properties of tissue, is demonstrated for *in vivo* detection of nonstenotic plaques and plaque material assessment in this pilot investigation. *In vivo* ARFI imaging was performed on four iliac arteries: 1*)* of a normocholesterolemic pig with no atherosclerosis as a control, 2) of a familial hypercholesterolemic pig with diffuse atherosclerosis, 3) of a normocholesterolemic pig fed a high-fat diet with early atherosclerotic plaques and 4) of a familial hypercholesterolemic pig with diffuse atherosclerosis and a small, minimally-occlusive plaque. ARFI results were compared to spatially matched immunohistochemistry, showing correlations between elastin and collagen content and ARFI-derived peak displacement and recovery time parameters. Faster recoveries from ARFI-induced peak displacements and smaller peak displacements were observed in areas of higher elastin and collagen content. Importantly, spatial correlations between tissue content and ARFI results were consistent and observable in both large and highly evolved as well as small plaques. ARFI imaging successfully distinguished nonstenotic plaques, while conventional B-Mode ultrasound did not. This work validates the potential relevance of ARFI imaging as a noninvasive imaging technology for *in vivo* detection and material assessment of atherosclerotic plaques.

Corresponding Author: Russell H. Behler Pre-Doctoral Candidate Joint Department of Biomedical Engineering, University of North Carolina at Chapel Hill and North Carolina State University 150 MacNider Hall Chapel Hill NC, 27599 USA russbehler@unc.edu phone: 919-843-6647.

Keywords

acoustic radiation force; ultrasound; atherosclerosis; detection; characterization; collagen; elastin; pig model

Introduction

Cardiovascular disease (CVD) is the leading cause of death globally; the majority of CVD deaths are due to sequelae of atherosclerosis (WHO fact sheet no. 317, February 2007). Atherosclerosis is routinely diagnosed by a variety of imaging methods (Sanz *et al* 2008, Rosamond *et al* 2008, Mackay and Mensah 2004). These methods include invasive techniques such as coronary angiography and intravascular ultrasound (IVUS), as well as noninvasive approaches such as ultrasound carotid intima-media thickness (CIMT) measures. These imaging methods are known to be effective for detecting occlusive plaques associated with pronounced narrowing of the vessel lumen and/or blood flow obstruction (known as 'stenotic' plaques). However, they are not demonstrated for detecting nonstenotic plaques or for characterizing plaque material composition (Glagov 1987; Libby and Theroux 2005, Raggi *et al* 2005). It is well established that certain material characteristics, such as a large lipid pool and a thin or disrupted fibrous cap, are indicative of increased plaque vulnerability (Rader *et al* 2008, Gerszten *et al* 2008, Nighoghossian *et al* 2007). Nonstenotic plaques, particularly those with soft lipid cores and thin or disrupted fibrous caps, are associated with risk for initiating ischemic events. There is a clear yet unmet need for a validated atherosclerosis imaging modality that can improve nonstenotic plaque detection and predict cardiovascular risk.

Rather than assessing luminal narrowing, atherosclerosis imaging approaches capable of describing plaque composition, size, structure, and mechanical properties – material features that are known to influence plaque stability - are gaining significance in current research with potential to translate into clinical diagnostics (Sanz *et al* 2008). Imaging techniques in practice and under development that aim to materially characterize atherosclerotic plaques include X-ray computed tomography (CT) (Raggi *et al* 2005; Schuijf *et al* 2006), magnetic resonance imaging (MRI) (Yuan *et al* 2006), intravascular ultrasound (IVUS) integrated backscatter (IB) and virtual histology (VH) methods (Amano *et al* 2007; Boese *et al* 2004; Bose *et al* 2007; Granada *et al* 2006, Nair *et al 2002*), and IVUS elastography (De Korte *et al* 2002; Baldewsing *et al* 2006; Saijo *et al* 2006). Although IVUS offers many advantages over angiography, its widespread use in clinical practice may be partially limited by its invasive nature, which carries a certain level of risk (Pulido *et al* 2004; Bose *et al* 2007).

Novel noninvasive approaches to detecting and materially characterizing atherosclerotic plaques include acoustic radiation force based methods. Such methods exploit energy in transmitted acoustic pulses to deliver localized, precise force sufficient in magnitude to induce subtle tissue displacements. Induced displacements can be tracked using conventional ultrasonic means, and they are indicative of local tissue mechanical, *i.e*. material, properties (Nightingale *et al* 2002; Palmeri *et al* 2005b). Radiation force-based methods have been demonstrated in recent years for differentiating tissue structure via mechanical property in varied applications, including discrimination of breast lesions (Alizad *et al* 2004; Soo *et al* 2006), myocardial RF ablations (Fahey *et al* 2005a), abdominal aortic aneurysms (Mozes *et al* 2005), thermally and chemically induced lesions (Bercoff *et al* 2004), abdominal organs (Fahey *et al* 2005b), the gastrointestinal track (Palmeri *et al* 2005a), liver (Nightingale 2006), thrombosis (Viola *et al* 2004), and myocardium (Bradway *et al* 2007; Hsu *et al* 2007). In addition, acoustic radiation force has been effective for delineating tissue structure in human peripheral arteries (Dahl *et al* 2006; Trahey *et al* 2004)

as well as pig arteries (Pislaru et al 2008; Zhang and Greenleaf 2007; Zhang *et al* 2006). We recently published our results of *ex vivo* Acoustic Radiation Force Impulse (ARFI) imaging in a familial hypercholesterolemic (FH) pig iliac artery with confirmation of ARFI findings by matched immunohistochemistry (Dumont *et al* 2006).

This paper extends our previous *ex vivo* demonstration (Dumont *et al* 2006) to *in vivo* application of ARFI ultrasound for materially characterizing atherosclerotic plaques in a relevant pig model of atherosclerosis. ARFI results are spatially correlated to tissue collagen and elastin composition.

Both elastin and collagen are important to overall plaque stability. Elastin, a significant component of the extracellular matrix of large blood vessels, enables arterial dilation and contraction in response to variations of blood pressure while collagens, the major proteins of the extracellular matrix, form fibrils and networks that resist tensile stress (Goncalves *et al* 2007). Plaque collagen and elastin content is the net result of dynamic balances between synthesis and degradation.

Elastin synthesis is common in plaques associated with symptoms; morphological studies suggest that coronary plaques associated with unstable angina have increased intimal elastin content compared with stable plaques. Carotid plaques associated with ipsilateral hemispheric symptoms had 30% higher amounts of elastin compared with plaques not associated with symptoms. On the other hand, increased elastolytic activity is associated with severity of atherosclerosis in the aorta. Beyond mechanical stability, elastin plays a role in the pathogenesis of atheroclersosis. Elastin appears to bind cholesterol so strongly that the bound cholesterol cannot be removed by HDL, and the permeability of the elastic lamina can affect the rate of lipoprotein entrapment (Goncalves et al 2007).

Collagen synthesis occurs very early in lesion development and may represent the major mechanism of lesion progression. Collagen is degraded by matrix metalloproteinases and other enzymes secreted by inflammatory cells. Excessive collagen leads to arterial stenosis, while insufficient collagen makes atherosclerotic plaques prone to rupture. Collagen may also stimulate further lesion progression by serving as a depot for proatherogenic molecules: modified lipoproteins, growth factors, and glycation end-products. Collagen can modulate macrophage functions, smooth muscle cell proliferation, migration, and responsiveness to growth factors, and stimulate thrombus formation (Rekhter 1998). Monitoring plaque composition is important to diagnosing atherosclerosis and assessing cardiovascular risk, and delineating collagen and elastin content may promote earlier plaque detection than possible by conventional atherosclerosis imaging technologies.

With this knowledge of the influence of collagen and elastin on atherosclerotic plaque progression and stability, and based on our previous *ex vivo* results, we hypothesize that *in vivo* ARFI imaging parameters - time to recovery from peak ARFI-induced tissue displacement and peak ARFI-induced tissue displacement - are statistically correlated with tissue elastin and collagen content. This finding would be relevant to improved detection of nonstenotic plaques and to description of plaque stability believed to be conferred by elastin and collagen degradation and deposition.

Third, a linear regression model was used to calculate the correlation between median ARFI parameter values and elastin and collagen fractional area. P-values were calculated using Student’s t distribution (by the *corr* function in MATLAB Statistical Toolbox, MathWorks, Inc.)

Methods

Familial Hypercholesterolemic (FH), Dietary Hypercholesterolemic (DH), and Normocholesterolemic (NC)Pigs

FH pigs spontaneously exhibit hypercholesterolemia (~range 350 to 500 mg/dl) when eating low fat pig feed due to a missense mutation in the LDL receptor (Grunwald *et al* 1999, Hasler Rapacz *et al* 1998). DH pigs are normocholesterolemic pigs that, when fed a high fat diet, develop hypercholesterolemia that is comparable to the FH pigs (Nichols *et al* 1990; Nichols *et al* 1992; Nichols *et al* 1999; Brodala *et al* 2005; Nichols *et al* 2007). Most importantly, both the FH and DH strains develop atherosclerotic lesions that recapitulate the histopathology seen in humans: proliferative lesions consisting of smooth muscle cells, macrophages, lymphocytes, foam cells, calcification, fibrous caps, medial thinning, intimal thickening, necrotic and apoptotic cells, plaque hemorrhage, and expanded extracellular matrices with alterations in collagen and elastin content (Gerrity *et al* 1979, Prescott *et al* 1991, Nichols *et al* 1992, Prescott *et al* 1995, Brodala *et al* 2005). NC pigs have normal LDL receptor and have a serum cholesterol range of 60 to 120 mg/dl when fed the same low fat pig feed that is fed to the FH pigs. NC pigs do not develop atherosclerosis and thus serve as valid experimental controls to the FH and DH pigs. Imaging was performed *in vivo* on the iliac arteries of four pigs: a 3 years, 6 months old NC control female, a 4 years, 4 months old FH female, and a 3 years, 1 month old DH female, and a 8 years, 4 months old FH female.

Ultrasonic Imaging and data processing

Two-dimensional B-Mode and ARFI imaging were performed with a Siemens Sonoline Antares™ Ultrasound Scanner (Siemens Medical Solutions USA, Inc. Ultrasound Division) using a VF7-3 linear array transducer. ARFI impulses were 300 cycles in duration administered at a 4.21 MHz center frequency with an F/# 1.5 focal configuration. ARFI tracking pulses were conventional 2-cycle B-Mode transmit-receive (TX-RX) A-lines at a center frequency of 6.15 MHz with an 11 kHz pulse repetition frequency. The ARFI beam sequence for the first three examples acquired 40 ensembles spaced 0.53 mm apart, generating an effective lateral FOV of 2.1 cm. In the fourth example, 15 lateral positions were interrogated using 4:1 parallel RX tracking, giving 60 effective lateral positions spaced 0.35 mm apart with a lateral FOV of 2.1 cm. Each ARFI ensemble consisted of two 2-cycle TX-RX reference pulses followed by a 300-cycle (~70 μs) excitation impulse and then 60 subsequent 2-cycle TX-RX tracking pulses (for a tracking duration of 6 ms). One-dimensional cross correlation was applied to the acquired RF data ensembles to measure axial ARFI-induced displacements. We conservatively estimate tissue heating associated with this ARFI beam sequence to be < 1°C (Palmeri *et al*. 2004). As an additional precaution against additive heating as well as interfering displacements, wiperblading was employed as described in Dumont *et al*. (2006). One spatially matched B-mode frame was acquired immediately prior to each 2D ARFI acquisition for anatomical reference. From the acquired ARFI data, two parametric images were generated, an image of peak ARFI-induced displacement and an image of time to 67% recovery from peak ARFI-induced displacement. The 67% recovery metric is approximated as the time when full tissue recovery from displacement has been reached (Nightingale et al. 2002).

Physiological motion was rejected using a novel filter based on the quasi-static rigid wall (QSRW) model (Behler *et al* 2007; Fung 1993; Womersley 1955; Kuiken 1984). Briefly, the QSRW model suggests that arterial wall segments experience bulk motion in response to cardiac pulsation. Over the ensemble separation distances applied in ARFI imaging (~1cm), we assume continuous displacement from cardiac motion over the collected ensembles. According to this model, ARFI sequences were assembled into a global displacement curve, such that the final measured displacement of one ensemble became the starting displacement

for the next ensemble. A 20th order polynomial was then fit to this global displacement curve for each depth position, producing an approximation for the gross physiological motion observed during the entirety of ARFI imaging. The resulting polynomials were then subtracted from ARFI displacement profiles to correct for physiologic motion while preserving ARFI-induced displacements (Behler *et al* 2007).

A luminal mask was applied to parametric ARFI images to reject displacements from blood, which streams in response to ARFI excitation and appears as noise in parametric ARFI images. The mask was created from a combination of two calculations: a thresholding algorithm and a correlation-based algorithm. The thresholding mask was generated from the matched B-Mode image, mapping relatively low amplitude regions to zero displacements as described in (Dumont *et al* 2006). The correlation-based mask used a median image of the correlation measurement from the last five tracking lines in each ensemble. Any location in the FOV with a median correlation less than the empirically derived threshold (0.992) was discarded. The two masks were then multiplied to generate a single effective mask. Using the luminal mask as a basis, remaining unmasked portions of lumen were removed by hand in parametric ARFI images.

Histology

The pigs were sedated prior to imaging in the lateral decubitus position, with the lower extremities extended to provide acoustic access to the iliac arteries in the inguinal canal. The location of the transducer on the surface of the skin was marked with a tattoo following imaging by a professional sonographer. This tattoo supported spatial registration of the vessels extracted from the pigs at necropsy, which occurred within 48 hours of imaging.

Harvested vessels were opened longitudinally, with the near and far walls seen in ARFI imaging positioned one quarter and three quarters down the circumferential length of the iliac, respectively. These regions were then sectioned for immunohistochemical analysis with assistance from a pathologist who observed imaging procedures. Three sections spaced 10 μm apart were stained with hematoxylin and eosin (H&E) for baseline, Masson's Trichrome (MT) for collagen, and Verhoeff von Gieson (VVG) for elastin. In the case of the DH pig, sections were also stained with Sirius Red (SR) for differentiation of collagen subtypes I and III as demonstrated by Junquiera *et al* (1978, 1979). All histology sections were imaged with transmission light microscopy, and the SR stained sections were also imaged with linearly polarized light microscopy. All procedures were approved by the University of North Carolina at Chapel Hill Institutional Animal Care and Use Committee (IACUC).

To spatially correlate histology to ARFI images, we adopted methods previously established by Yuan *et al* (2005). These researchers spatially registered histology from carotid endarterectomy specimens to MR images by noting distance to identifiable landmarks and gross arterial and plaque morphological features for reference at necropsy and sectioning. We acknowledge that minor misalignments may occur; however, with the exception of cases involving very high spatial frequency variations in tissue composition, we do not expect misregistration to be significant source of error.

Statistical Analysis

For arteries containing plaques, parametric ARFI recovery time and peak displacement measurements were separately correlated with to immunohistochemical collagen and elastin content. First, in parametric ARFI images, the arterial wall of interest was isolated from surrounding tissue. The median parameter value over the axial range of the arterial wall and an empirically determined lateral span, L (ranging from 1.0 to 2.0 mm), was then calculated.

A vector of median parameters values was calculated by stepping the parameter calculation window laterally across the arterial wall with a step-size of one lateral ARFI imaging position (0.5 mm).

Second, in the corresponding immunohistochemical images, the vessel wall was isolated from background. Local percentages of collagen or elastin composition were then calculated as follows: First, a segment that encompassed the entire wall thickness and lateral span *L* was subdivided on the left-most side of the image. A color threshold was then applied to the image segment using NIH ImageJ with the colour threshold plugin (Rasband 2007). The colors black (in VVG stain for elastin) and blue (in MT stain for collagen) were individually differentiated. Elastin and collagen fractional areas were then calculated as the number of black or blue pixels divided by the total number of arterial wall pixels in the segment. A vector of collagen and elastin fractional area values was calculated by stepping the segment of interest laterally across the arterial wall with a step-size of 0.5 mm. In this manner, percent area calculations were spatially matched to median ARFI parameter calculations. Edge effects were accounted for by increasing the size of the segment of interest from *L*/2 by 0.5 mm to *L*.

Results

In Vivo Left Normocholesterolemic (NC) Control Pig Iliac Artery

A B-mode of the left iliac of a normal lipid control pig (Fig. 1, panel a) shows a clearly defined vessel wall with no intimal-medial wall thickening and no luminal narrowing suggesting no identifiable atherosclerosis. Imaging was focused to the position of the far vessel wall at 36 mm. Tissue corresponding to the far wall in B-Mode imaging is indicated by the yellow rectangle in the *en face* image of the vessel (Fig. 1, panel b). The width of the rectangle is approximately matched to the elevational resolution of the imaging system (~ 1 mm). The black line inside the yellow rectangle corresponds to the location sectioned for histology. Examining the *en face* vessel revealed no apparent atherosclerosis. This was confirmed by histology staining, as seen in the VVG stained section indicating elastin in black (Fig. 1, panel c) as well as the MT stained section, indicating collagen in blue (Fig. 1, panel d). The parametric ARFI imaging showing time to recovery (Fig. 1, panel e) indicates that the response of the distal vessel wall (boxed) is approximately the same (2.75 to 3 ms) across the lateral span of the image. Similarly, the distal wall (boxed) in the parametric ARFI peak displacement image (Fig. 1, panel f) experiences uniform peak displacement (~1 μm) in response to ARFI excitation. This is consistent with the uniform elastin and collagen content observed in panels c and d.

In Vivo Left FH Pig Iliac Artery

In contrast to the control vessel shown above, the left iliac artery of a female FH pig did contain an atherosclerotic plaque. In the B-Mode image of Fig. 2 panel a, subtle intimal-medial wall thickening and non-critical luminal narrowing of less than 10% are apparent (red arrows). Although the B-Mode image does not indicate advanced atherosclerosis, the excised vessel showed diffuse atherosclerosis throughout the extracted segment. The segment is shown *en face* with the lumen exposed in panel b. A yellow rectangle indicates the near arterial wall, where imaging was focused, and a thin black line shows the area of sectioning for staining with H&E, VVG, and MT.

VVG staining results are displayed in panel c, with the proximal wall segmented into three boxes that together span the imaging FOV. Box 1, the region corresponding to the left portion of the near wall in imaging, shows a degraded internal elastic lamina (IEL) (black stain, black arrows) with increasing elastin deposition at the position of the IEL from left to

right. On the luminal side of the IEL lies what appears to be a pool of foam cells (no stain, red arrow) and a fibrous cap (yellow arrow). The region indicated by box 2 highlights a significantly different plaque structure and composition. In this region there is extensive elastin deposition (black stain, black arrows) except in one notable location (green arrow). This complex and highly developed atherosclerotic plaque exhibits a complex cellular structure with severe medial thinning; however, the plaque does not protrude any further into the lumen than the tissue in either box 1 or box 3. It is an advanced nonstenotic plaque. Box 3 shows a consistent and nearly intact IEL and no significant elastin deposition.

The section stained with MT is displayed in panel d and is segmented into three boxes spatially matched to those of panel c. Box 1 exhibits a progressive increase in collagen deposition moving from left to right at the position of the IEL (blue stain, arrows). Box 3 shows a fairly homogeneous collagen deposition layer (arrows). Box 2, however, shows extensive collagen deposition throughout the complex nonstenotic plaque.

Corresponding ARFI results for the *in vivo* FH pig are displayed in Fig 3, including spatially matched boxes highlighting the same 3 ROIs as Fig 2. Time to recovery from peak ARFI-induced displacement is shown parametrically in panel a, with color mapping recovery time in ms. In box 1, the recovery time decreases from left (~4 ms, red) to right (~2.5 ms, green), which spatially corresponds to the progressive deposition of elastin seen in Fig. 2, panel c, box 1 and of collagen seen in Fig. 2, panel d, box 1. In box 2 of Fig 3, panel a, there is a fairly uniform recovery time across the entire box (~1.5 ms, blue), except for the small region illustrated by a white arrow (~4 ms, red), which spatially corresponds to the region lacking elastin deposition (green arrow in Fig 2, panel c, box 2). Note that recovery time in box 2 is generally much faster than in boxes 1 or 3, which spatially corresponds to more elastin and collagen deposition in box 2. Box 3 of Fig 3, panel a shows a uniform recovery time (~3.5 ms, orange) across the entire region of interest, consistent with the intact IEL and uniform collagen layer seen in Fig 2, panels c and d, box 3.

Peak ARFI-induced displacements are shown in the parametric image in panel b of Fig. 3, with color denoting displacement in μm. Box 1 shows a gradual decrease in overall peak displacement from left to right (~2.5 to 1.5 μm, red to green), which is spatially consistent with the progressive deposition of elastin and collagen seen in Fig 2, panels c and d, box 1. Box 2 of Fig 3, panel b exhibits smaller peak displacement (~0.75 to 1.25 μm, blue), consistent with the extensive elastin and collagen deposition shown in Fig 2, panels c and d, box 2. Finally box 3 shows a uniform peak displacement measurement (~1 μm, light blue) that is larger than box 2 but smaller than box 1, again consistent with the relative elastin and collagen distributions seen in Fig 2, panels c and d.

Scatter plots of median ARFI parameter values versus spatially matched tissue elastin and collagen fractional area are shown in Figure 4. Panel a illustrates recovery time vs. elastin, panel b peak displacement vs. elastin, panel c recovery time vs. collagen, and panel d peak displacement vs. collagen. Note that all four plots show an inverse relationship between tissue material (elastin or collagen) and ARFI parameter (recovery time and peak displacement), *i.e*. as tissue elastin and collagen content increase, recovery time and peak displacement decrease. Least squares linear fit lines are superimposed on the plots. The pairwise linear correlation coefficients, Rho, and P-values are reported in Table 1 below. Note that because elastin and collagen depositions are co-located in this example, it is not possible to statistically evaluate their separate impacts on tissue response to ARFI excitation. We elaborate on this limitation in the Discussion section.

In Vivo Left DH Iliac Artery

In Figure 5 panel a, a B-mode image of the left iliac artery of a DH pig shows no IMT or luminal narrowing, suggesting that no atherosclerosis is present. Imaging was focused to the position of the near arterial wall. The extracted vessel is shown *en face* (Fig. 5, panel b) with focal atherosclerotic plaques outlined in red. Although these focal plaques are not readily discernable in the digital photo of panel b, their presence and location was noted by palpation and visual inspection. The region of the vessel appearing as the near wall in imaging is denoted by a yellow rectangle drawn to approximate scale of the elevational beam width. Note that the plane of imaging passed through two focal atherosclerotic plaques (green and blue arrows). In the leftmost portion of the imaging FOV, the plane of imaging passed through the edge of a small, focal plaque (blue arrow, panel b). Slightly to the right of center, the imaging plane passed through a second, larger focal plaque (green arrow, panel b). Tissue in this region was sectioned as indicated by the black line (panel b) and stained with H&E, VVG, MT and SR as shown in panels c-e, respectively (H&E not shown). Initial inspection of immunohistochemistry sections suggests that the small plaque indicated by the blue arrow in panel b lacked sufficient structure to remain intact during the process of sectioning prior to staining. This is evidenced by small portions of debris in the region of the plaque, as shown in the immunohistochemistry stains (panels c-e), particularly in the SR stain (blue arrow, panel e).

Detail of the VVG stain for elastin (black) is shown in Figure 6, with 6 regions of interest shown at higher magnification to highlight the IEL (black arrows). Boxes numbered 1-6 correspond to the numbered regions indicated on the full sized section shown below the boxes. Box 1 shows a degraded IEL. Remnants of the detached focal plaque are also apparent (blue arrow). Box 2 shows a largely intact, though thin IEL. Box 3 shows increased intimal thickening with a more severely degraded IEL. Box 4, a region from the thickest portion of the second focal atherosclerotic plaque, exhibits a thin and highly degraded IEL. Box 5 shows a small gap in the IEL (red arrow); however the IEL generally remains intact and is thicker than the IEL in boxes 1-4. Box 6 shows an intact IEL comparably thick to the IEL shown in box 5.

Figure 7 displays MT stain of the six boxed regions of interest (spatially matched to those of Fig. 6) to highlight collagen composition (blue stain, black arrows). Boxes 1 -3 show a thin layer of collagen deposition, with slightly higher collagen deposition seen in box 3 coincident with more intimal layer thickening. Box 4, which contains the thickest region of the second focal plaque, shows a region of dense collagen deposition (dark blue stain, black arrows) in addition to a wider area of loose collagen deposition closer to the lumen (light blue stain, green arrows). Box 5 shows a thick, dense layer of collagen deposition, while box 6 shows collagen deposition similar to that of box 3.

Further analysis of collagen composition is available *via* linearly polarized light microscopy of the SR section, as shown in Figure 8. In polarized microscopy of SR stain, collagen type I fibers appear red, and collagen type III fibers appear green. Type I fibers are generally thicker are more stiff than type III fibers (Rubin and Farber 1994). The entire tissue section is shown at bottom in Fig. 8 with labeled regions of interest. The labels are numbered to indicate spatial alignment with magnified regions of interest presented in Figs. 6 and 7. Box 4.5 corresponds to a tissue region positioned between boxes 4 and 5 in Figs. 6 and 7.

Box 1 - adventitia of Fig. 8 illustrates the relative high collagen type I fiber content consistent with adventitial tissue (red stain, white arrows); some type III fibers (green stain) are intertwined with the type I fibers. In box 1 - intima, which contains a portion of the small plaque on the left side of the imaging FOV (Fig 5, panel b, blue arrow), collagen deposition is mostly in the form of type III fibers (green stain, blue arrow), with type I fibers

intertwined. Box 4, which contains a portion of the second focal plaque (Fig 5, panel b, green arrow), shows that the tissue is predominantly comprised of type III fibers (blue arrows). Conversely, boxes 4.5 and 5, show a higher type I fiber content, with more densely packed fibers.

ARFI imaging results are shown in Fig. 9, with time to recovery shown in panel a and peak displacement shown in panel b. Numbered boxes spatially matched to those of Figs. 6 and 7 are shown in both panels. The time to recovery image (panel a) is shown on a color scale of ms, while the peak displacement image (panel b) is on a scale of μm. In the time to recovery image, tissue in boxes 1, 3 and 4 (where the IEL is thin and degraded) exhibits relatively slow recovery (~3 to 4 ms). In contrast, tissue in boxes 5 and 6 (where the IEL is thicker and generally intact) shows a faster recovery of ~2 – 2.5 ms. In the peak displacement image (panel b), tissue in boxes 4 and 5 exhibit the smallest ARFI-induced peak displacement, consistent with the larger collagen deposition in this region. More specifically, tissue in box 4 displaces slightly more (~0.75 μm) than tissue in box 5 (~ 0.25 μm), which is consistent with the higher collagen type III fiber content in box 4.

The scatter plots of Fig. 10 illustrate the relationship between spatially matched median ARFI parameter values and tissue elastin and collagen content. Again, the least squares linear fits are superimposed on the graphs, with recovery time and peak displacement vs. elastin shown in panels a and b, and recovery time and peak displacement vs. collagen in panels c and d, respectively. The corresponding Rho and P-values are reported in Table 1, column 2. The single statistically relevant correlation is between peak displacement and collagen fractional area; however, our statistical methods do not take into account the structure of the IEL. Further discussion of this limitation is provided below.

In Vivo Left FH Iliac Artery 2

In Fig. 11 panel a, a B-Mode image of the left iliac artery of a second FH pig shows what appears to be a focal plaque (orange arrow) with minimal luminal narrowing and intimal-medial wall thickening in the surrounding vessel wall. Imaging was focused on the distal wall at 28mm. The *en face* image (panel b) shows diffuse atherosclerosis, which was collaborated by visual inspection and palpation. Tissue appearing as the far wall in the B-Mode image is surrounded by the yellow box in panel b, and histology sections were taken from the region indicated by the black line.

Examining the histology sections stained for H&E (panel c), VVG (panel d), and MT (panel e) confirms the presence of diffuse atherosclerosis. Though the amount of vessel wall thickening is relatively constant, two atheromatous plaques are visible (green and red arrows). The plaque highlighted by red arrows is covered by a degraded fibrous cap, as indicated by the break in collagen above the atheromatous core (yellow arrow, panel e). Interestingly, heightened collagen deposition is apparent in the arterial wall around this plaque (darker blue). The second atheromatous plaque (highlighted by green arrows) exhibits a thick, intact fibrous cap, which is evident as a layers of collagen (panel e) and elastin (panel d) in MT and VVG stains, respectively. The atheromatous core below the fibrous cap is large and collagen free, although it appears to contain a region of mineralization consistent with calcification. This is supported by the large black region in H&E (blue arrow, panel c) and VVG (blue arrow, panel d) stains. To confirm calcification, a tissue section was stained with Alizarin Red. The result, shown in panel f, verifies that the region highlighted by the yellow arrow is calcification (blue arrow, panel f) rather than elastin deposition. Lastly, disruption in IEL (panel d) on the left side of the vessel wall is highlighted by a black arrow.

The spatially matched parametric ARFI images are shown in Fig. 12, with recovery time in panel a and peak displacement in panel b. Panel a shows a relatively consistent recovery time for the distal wall (~1 ms, panel a) with two exceptions. First, a region of slow recovery (black arrow, ~2 ms) spatially corresponds to the disruption in the IEL highlighted by black arrows in Fig. 11. Second, a region of fast recovery (orange arrow, ~0.6 ms) spatially corresponds to the thick, intact fibrous cap observed above the right atheromatous plaque, which contained both elastin and collagen (Fig. 11, green arrows). The parametric ARFI peak displacement image (panel b) also shows a fairly uniform arterial wall response to ARFI excitation (~2 -2.5 μm peak displacement), with the exception of the region highlighted by the orange arrow. This region, which exhibits relatively large peak displacement (> 6 μm), spatially corresponds to the atheromatous core of the right plaque (Fig. 11, green arrows).

Scatter plots illustrating the relationship between tissue elastin and collagen content and median ARFI parameter values are shown in Fig. 13. Table 1, column 3 reports the corresponding Rho and P-values. Note that black pixels corresponding to calcium deposition (as confirmed by Alizarin Red stain) were neglected prior to elastin fractional area calculation. The single statistically relevant correlation is between peak ARFI-induced tissue displacement and tissue collagen content. However, we again neglect the impact of the structure of IEL in this analysis, and elastin and collagen depositions are co-located in the intact fibrous cap. The impact of this is discussed below.

Discussion

The results of this pilot *in vivo* investigation show a relationship between tissue elastin and collagen composition and peak displacement and recovery time in response to ARFI excitation. In a negative control example, uniform ARFI peak displacement and recovery time results correspond to negligible variations in tissue elastin and collagen composition (Fig. 1). In a highly evolved and complex nonstenotic plaque, elastin and collagen deposition was statistically correlated with decreased ARFI recovery time and peak displacement (Figs. 2-4; Table 1, column 1). Importantly, it is this differential ARFI result that enables identification of the nonstenotic yet highly evolved plaque that was not evident by conventional B-Mode imaging. Based on our understanding of the physiological roles of elastin and collagen in atherosclerosis, and based on our previous *ex vivo* findings (Dumont *et al* 2006), we hypothesize that elastin dominates ARFI recovery time and collagen dominates ARFI peak displacement. However, it is not possible to examine the independent effects of elastin and collagen in this study design. This is due to the fact that elastin and collagen deposition are co-located in this example. More specifically, where there is elastin deposition, there is also collagen deposition.

Without consideration of this critical fact, the scatter plots of Fig. 4 may be misleading. While there appears to be a statistically significant correlation between decreased peak displacement *and* recovery time and elastin deposition (panels a and b; Table 1, column 1), one must be conscious of the fact that collagen is also deposited. Similarly, while Fig. 4 seems to show a statistically significant correlation between decreased peak displacement *and* recovery time and collagen deposition (Fig. 4 panels a and b; Table 1, column 1), one must be aware that elastin is also deposited. We hypothesize that the apparent correlations between peak displacement and elastin and recovery time and collagen are predominantly artificial results. To fully test our hypothesis, atherosclerotic examples of elastin and of collagen deposition alone are needed.

In the case of small, focal plaques that were not apparent on conventional B-Mode ultrasound but were discernable by ARFI imaging, only collagen deposition was statistically

correlated to decreased ARFI peak displacement (Figs. 5-10; Table 1, column 2). While this result is consistent with our expectation for tissue collagen content, we acknowledge that our statistical analysis of elastin is flawed in that we do not take into account the structure of the IEL. It is well established that the IEL gives arterial walls structure and stability and that disruption of the IEL in atherosclerosis promotes plaque vulnerability (Moreno et al 2002). However, our analysis considers only elastin fractional area. Although the IEL is thin, and therefore does not constitute a large fractional area of the arterial wall, we hypothesize that its organization and intact status impacts ARFI recovery time more than unstructured elastin deposition. However, in this investigation, we overlook IEL structure. A formal ROC analysis using readers trained to recognize slow recovery times as possible disruptions in the IEL will allow us to evaluate the relevance of IEL structure to ARFI outcomes.

In the case of diffuse atherosclerosis with two atheromatous plaques, only collagen deposition was statistically correlated with peak displacement in this example (Figs. 11-13; Table 1, column 3). However, we again neglect the structure of the IEL in our analysis. Interestingly, only one of the two atheromatous plaques was apparent by conventional B-Mode ultrasound (as a minimally stenotic plaque; Fig. 11) and by ARFI imaging (as a structure with a highly displaceable center with a fast recovering, low displacing cap, Fig. 12). Although differences in tissue material content allowed ARFI to identify the right plaque as atheromatous, the left plaque was missed by both B-Mode and ARFI imaging. We hypothesize that the disrupted fibrous cap associated with the left atheromatous plaque is an indication of necrosis and that surrounding collagen deposition stabilizes the plaque. Therefore, the plaque does not exhibit an identifiably different response to ARFI excitation than the surrounding arterial wall tissue. This points out a critical limitation to ARFI imaging of atherosclerosis – while ARFI imaging effectively exploits differences in tissue mechanical, *i.e*. material, properties to reveal underlying plaques, in the context of homogeneous material composition and/or mechanical response, ARFI performance may be compromised.

An additional limitation to ARFI atherosclerosis imaging using our current methods is depth of penetration, which currently limits ARFI to peripheral vascular applications. While atherosclerosis assessment in peripheral vessels, such as the carotid, is certainly clinically relevant (for stroke risk assessment and for indication of coronary artery disease, for example (Ashrafian *et al* 2006)), ARFI could be realizable for coronary artery imaging *via* alternative imaging transducers. Importantly, interventions in pigs have been regarded as having a positive predictive value for subsequent translation to human atherosclerosis (Johnson et al 1999). Note that the pig model is humanoid both in terms of the nature of atherosclerosis it develops and in terms of the size and geometry of its peripheral vasculature. We therefore anticipate that ARFI imaging results achieved in the pig model will be directly translatable to humans.

Finally, it critical that the results presented here be considered in the context of the pilot nature of this work. Although our preliminary results support our hypothesis that *in vivo* ARFI imaging recovery time and peak displacement parameters are statistically correlated to tissue elastin and collagen content, we have not examined a sufficient number of pigs to definitely establish ARFI's ability to differentiate collagen and elastin composition in atherosclerotic plaques. Rather, these results serve to 1) demonstrate feasibility of *in vivo* ARFI imaging in the FH, DH, and NC pigs with spatially matched immunohistochemical processing, 2) substantiate early (though incomplete) support of our hypothesis that there is a relationship between ARFI recovery time and peak displacement parameters and tissue elastin and collagen composition in three different plaque types, and 3) generate data for realization of critical strengths and weaknesses in our experimental protocol for future work.

Conclusions

In a pilot survey of three different atherosclerotic plaque types, 1) a complex and highly evolved nonstenotic plaque, 2) small, focal plaques, and 3) atheromatous plaques, we demonstrate ARFI ultrasound for noninvasive material characterization of atherosclerotic plaques, *in vivo*. With spatially matched immunohistochemistry, we show a spatial correlation between arterial wall elastin and collagen content and ARFI recovery time and peak displacement results. In regions of increased elastin and collagen deposition, smaller ARFI recovery times and peak displacements are observed. This differential response to ARFI excitation promoted identification of a nonstenotic plaque that was not evident on conventional B-Mode ultrasound, differentiation of small focal plaques that were not apparent by B-Mode, and description of an atheromatous plaque that appeared as a focal, minimally stenotic plaque on B-Mode. Statistical methods supported our general hypothesis that *in vivo* ARFI imaging recovery time and peak displacement parameters are correlated to tissue elastin and collagen content. However, our study design could not isolate the impact of co-located elastin and collagen deposition, and we neglected IEL structure in our analysis. Additional experiments including examples of elastin and collagen deposition alone and a formal ROC analysis are needed to fully evaluate the relationship between tissue elastin and collagen composition and tissue response to ARFI excitation. Nevertheless, the results reported here demonstrate that noninvasive, *in vivo* ARFI imaging is effective for identifying and materially characterizing atherosclerotic plaques that are missed or poorly described by conventional B-Mode ultrasound.

Acknowledgments

We thank Gregg Trahey, Jeremy Dahl, and Kathy Nightingale of Duke University for technical consultation. We also thank Siemens Medical Solutions USA, Inc. Ultrasound Division for *in kind* support. This work was supported by NIH grants 2K12HD001441-06, P20RR0207764-01, T32HL069768-05, AHA Grant 0765330U and a JBME RIP Grant.

References

Alizad A, Fatemi M, Wold LE, Greenleaf JF. Performance of vibro-acoustography in detecting microcalcifications in excised human breast tissue: A study of 74 tissue samples. IEEE Trans on Med Imag. 2004; 23:307–312.

Amano T, Matsubara T, Uetani T, Nanki M, Kato M, Arai K, Yokoi K, Ando H, Ishii H, Izawa H, Murohawa T. Impact of Metabolic Syndrome on Tissue Characteristics of angiographucally mild to moderate coronary lesions – Integrated backscatter intravascular ultrasound study. J. Am. Coll. Cardiol. 2007; 49:1149–1156. [PubMed: 17367657]

Ashrafian H, Lim T, Senior R. Carotid Ultrasound Imaging: An Effective Technique for Detecting Early Atherosclerosis – Vascular Screening for CVD has come of Age. Journal of the American Society of Echocardiography. 2007; 20:1–3. [PubMed: 17218195]

Baldewsing RA, Mastik F, Schaar JA, Serruys PW, van der Steen AF. Young's Modulus Reconstruction of Vulnerable Atherosclerotic Plaque Components Using Deformable Curves. Ultrasound Med Biol. 2006; 32:201–210. [PubMed: 16464666]

Behler, RH.; Dumont, DM.; Nichols, TC.; Merricks, EP.; Gallippi, CM. ARFI Ultrasound for Characterizing Atherosclerosis. IEEE Ultrasonics Symposium Proceedings; 2006. p. 722-727.

Behler, RH.; Nichols, TC.; Merricks, EP.; Gallippi, CM. A Rigid Wall Approach to Physiologic Motion Rejection in ARFI Imaging. IEEE Ultrasonics Symposium Proceedings; 2007.

Bercoff J, Pernot M, Tanter M, Fink M. Monitoring thermally-induced lesions with supersonic shear imaging. Ultrasonic Imaging. 2004; 26:71–84. [PubMed: 15344412]

Boese D, Shumermund A, Margolis P, Nair A, Vince G, Eggebrecht H, Naber C, Erbel R. Intravascular Ultrasound Radiofrequency Analysis identifies plaque composition: virtual histology. European Heart Journal. 2004; 25:20–20 Suppl. S.

Bose D, von Birgelen C, Erbel R. Intravascular Ultrasound for the Evaluation of Therapies Targeting Coronary Atherosclerosis. J. Am. Coll. Cardiol. 2007; 49:925–932. [PubMed: 17336714]

Bradway, DP.; Hsu, SJ.; Fahey, BJ.; Dahl, JJ.; Nichols, TC.; Trahey, GE. Transthoracic Cardiac ARFI: a Feasibility Study. IEEE International Ultrasonics Symposium; October 2007;

Brodala N, Merricks EP, Bellinger DA, Damrongsri D, Offenbacher S, Beck J, Madianos P, Sotres D, Chang YL, Koch G, Nichols TC. Porphyromonas gingivalis bacteremia induces coronary and aortic atherosclerosis in normocholesterolemic and hypercholesterolemic pigs. Arterioscler Thromb Vasc Biol. 2005; 25:1456–1451.

Chopra V, Choksi PU, Cavusoglu E. Beyond lipid lowering: The anti-hypertensive role of statins. Cardiovascular Drugs and Therapy. 2007; 21:161–169. [PubMed: 17468937]

Dahl JJ, Dumont DM, Miller EM, Schwark, Allen JD, Trahey GE. Characterization of in vivo atherosclerotic plaques in the carotid artery with Acoustic Radiation Force Impulse imaging. Proc. IEEE Ultrason Symp. 2006; 1:706–709.

de Korte CL, Sierevogel MJ, Mastik F, Strijder C, Schaar JA, Velma E, Pasterkamp G, Serruys PW, van der Steen AF. Identification of atherosclerotic plaque components with intravascular ultrasound elastography in vivo A Yucatan pig study. Circulation. 2002; 105:1627–1630. [PubMed: 11940537]

Dumont DM, Behler RH, Nichols TC, Merricks EP, Gallippi CM. ARFI Imaging for Noninvasive Material Characterization of Atherosclerosis. Ultrasound Med Biol. 2006; 32:1703–1711. [PubMed: 17112956]

Fahey BJ, Nightingale K, Wolf P, Trahey GE. Acoustic radiation force impulse imaging of myocardial radiofrequency abalation: Initial In vivo results. IEEE Trans Ultrason Ferroelec Freq Control. 2005a; 52:631–641.

Fahey BJ, Nightingale KR, Nelson RC, Palmeri ML, Trahey GE. Acoustic Radiation Force Impulse Imaging of the Abdomen: Demonstration of Feasability and Utility. Ultrasound Med Biol. 2005b; 31:1185–1198. [PubMed: 16176786]

Falk E, Prediman KS, Fuster V. Coronary Plaque Disruption. Circulation. 1995; 92:657–671. [PubMed: 7634481]

Franzen D, Sechtem U, Hopp HW. Comparison of angioscopic, intravascular ultrasonic, and angiographic detection of thrombus in coronary stenosis. Amer J Cardiol. 1998; 82:1273–1275. [PubMed: 9832106]

Fung, YC. Biomechanics: Mechanical Properties of Living Tissues. Springer; New York. NY: 1993.

Gerrity RG, Naito HK, Richardson M, Schwartz CJ. Dietary Induced Atherogenesis in Swine: Morphology of the Intima in Prelesion Stages. Am J Pathol. 1979; 95:775–792. [PubMed: 453335]

Gerrity RG, Natarajan R, Nadler JL, Kimsey T. Diabetes-induced accelerated atherosclerosis in swine. Diabetes. 2001; 50:1654–1665. [PubMed: 11423488]

Gerszten RE, Wang TJ. The search for new cardiovascular biomarkers. Nature. 2008; 451:949–952. [PubMed: 18288185]

Glagov S. Compensatory Enlargement of Human Atherosclerotic Coronary Arteries. N Engl J Med. 1987; 316:131–1375.

Gonçalves I, Moses J, Dias N, Pedro LM, Fernando JF, Nilsson J, Ares M. Changes Related to Age and Cerebrovascular Symptoms in the Extracellular Matrix of Human Carotid Plaques. Stroke. 2003; 34:616–622. [PubMed: 12624281]

Granada J, Wallace-Bradley D, Win H. In vivo Characterization Using Intravascular Ultrasound – Virtual Histology in a Porcine Model of Complex Coronary Lesions. Atherosclerosis, Thrombosis, and Vascular Biology. 2007; 27:387–393.

Grunwald K, Schueler K, Uelmen P, Lipton BA, Kaiser M, Buhman K, Attie AD. Identification of a novel Arg-->Cys mutation in the LDL receptor that contributes to spontaneous hypercholesterolemia in pigs. J Lipid Res. 1999; 40:475–485. [PubMed: 10064736]

Hasler-Rapacz J, Ellegren H, Fridolfsson AK, Kirkpatrick B, Kirk S, Andersson L, Rapacz J. Identification of a mutation in the low density lipoprotein receptor gene associated with recessive familial hypercholesterolemia in swine. Am J Med Genet. 1998; 76:379–386. [PubMed: 9556295]

Hasler-Rapacz JO, Nichols TC, Griggs TR, Bellinger DA, Rapacz J. Familial and diet-induced hypercholesterolemia in swine. Lipid, ApoB, and ApoA-I concentrations and distributions in plasma and lipoprotein subfractions. Arterioscler Thromb. 1994; 14:923–930. [PubMed: 8199183]

Hsu, SJ.; Hubert, JL.; Wolf, PD.; Trahey, GE. Acoustic Radiation Force Impulse Imaging of Mechanical Stiffness Propagation within Myocardial Tissue. IEEE UFFC International Ultrasonics Symposium; October 2007;

Ishimura E, Shoji T, Emoto M, Motoyama K, Shinohara K, Matsumoto N, Taniwaki H, Inaba M, Nishizawa Y. Renal insufficiency accelerates atherosclerosis in patients with type 2 diabetes mellitus. Am J Kidney Dis. 2001; 38:S186–190. [PubMed: 11576952]

Jaffer FA, Libby P, Weissleder R. Molecular and Cellular Imaging of Atherosclerosis Emerging Applications. J. Am. Coll. Cardiol. 2006; 47:1328–1338. [PubMed: 16580517]

Johnson GJ, Griggs TR, Badimon L. The utility of animal models in the preclinical study of interventions to prevent human coronary artery restenosis: analysis and recommendations. On behalf of the Subcommittee on Animal, Cellular and Molecular Models of Thrombosis and Haemostasis of the Scientific and Standardization Committee of the International Society on Thrombosis and Haemostasis. Thromb Haemost. 1999; 81:835–843. [PubMed: 10365761]

Junquira LC, Cossermelli W, Bretani R. Differential Staining of Collagens Type I, II and III by Sirius Red and Polarization Microscopy. Archiv Histol Jap. 1978; 41:267–274.

Junquira LC, Cossermelli W, Bretani R. Picosirius Staining Plus Polarization Microscopy, a Specific Method for Collagen Detection in Tissue Sections. Histochemical Journal. 1979; 11:447–455. [PubMed: 91593]

Kuiken GDC. Wave Propagation in a Thin-Walled Liquid-Filled Initially Stressed Tube. J. Fluid Mech. 1984; 141:289–308.

Libby P, Theroux P. Pathophysiology of coronary artery disease. Circulation. 2005; 111:3481–3488. [PubMed: 15983262]

Lima JC, Desai MY. Cardiovascular Magnetic Resonance Imaging: Current and Emerging Applications. J. Am. Coll. Cardiol. 2004; 44:1164–1171. [PubMed: 15364314]

Mackay, J.; Mensah, G. Atlas of Heart Disease and Stroke. World Health Organization; 2004.

Maurice RL, Doronat M, Ohayon J, Stoyanova E, Foster FS, Cloutier G. Non-Invasive High-Frequency Vascular Ultrasound Elastography. Physics in Med & Biol. 2005; 50:1611–28.

Moreno PR, Purushothaman KR, Fuster V, O'Connor WN. Intimomedial interface damage is increased beneath disrupted and adventitial inflammation atherosclerosis in the aorta - Implications for plaque vulnerability. Circ. 2002; 105:2504–2511.

Mozes G, Kinnick RR, Gloviczki P, Bruhnke RE, Carmo M, Hoskin TL, Bennet KE, Greenleaf JF. Noninvasive measurement of aortic aneurysm sac tension with vibrometry. J Vas Surg. 2005; 42:963–971.

Nagaraj A, Kim H, Hamilton A, Mun J, Smulevitz B, Kane BJ, Yan LL, Roth SI, McPherson DD, Chandran KB. Porcine carotid arterial property alterations with induced atheroma: an in vivo study. Medical Engineering and Physics. 2005; 27:147–156. [PubMed: 15642510]

Nair A, Kuban BD, Tuzcu EM, Schoenhagen P, Nissen SE, Vince DG. Coronary plaque classification with intravascular ultrasound radiofrequency data analysis. Circulation. 2002; 106:2200–2206. [PubMed: 12390948]

Nichols TC, Bellinger DA, Davis KE, Koch GG, Reddick RL, Read MS, Rapacz J, Hasler-Rapacz J, Brinkhous KM, Griggs TR. Porcine von Willebrand disease and atherosclerosis: Influence of polymorphism in apolipoprotein B100 genotype. Am J Pathol. 1992; 140:403–415. [PubMed: 1739133]

Nichols TC, Bellinger DA, Tate DA, Reddick RL, Read MS, Koch GG, Brinkhous KM, Griggs TR. von Willebrand factor and occlusive arterial thrombosis: A study in normal and von Willebrand's disease pigs with diet-induced hypercholesterolemia and atherosclerosis. Arteriosclerosis. 1990; 10:449–461. [PubMed: 2344301]

Nichols TC, Busby WH Jr. Merricks E, Sipos J, Rowland M, Sitko K, Clemmons DR. Protease Resistant IGFBP-4 Inhibits IGF-I Actions and Neointimal Expansion in a Porcine Model of Neointimal Hyperplasia. Endocrinology. 2007; 10:5002–5010. [PubMed: 17640990]

Nichols TC, du Laney T, Zheng B, Bellinger DA, Nickols GA, Engleman W, Clemmons DR. Reduction in atherosclerotic lesion size in pigs by alphaVbeta3 inhibitors is associated with inhibition of insulin-like growth factor-I-mediated signaling. Circ Res. 1999; 85:1040–1045. [PubMed: 10571535]

Nightingale, KR.; Zhai, L.; Dahl, J.; Frinkley, K.; Palmeri, M. Shear Wave Velocity Estimation Using Acoustic Radiation Force Impulsive Excitation in Liver In. IEEE Ultrasonics Symposium; 2006. p. 1156-1160.

Nightingale KR, McAleavey SA, Trahey GE. Shear wave generation using acoustic radiation force: *in vivo* and *ex vivo* results. Ultrasound Med Biol. 2003; 29:1715–1723. [PubMed: 14698339]

Nightingale KR, Soo MS, Nightingale RW, Trahey GE. Acoustic radiation force impulse imaging: in vivo demonstration of clinical feasibility. Ultrasound Med Biol. 2002; 28:227–235. [PubMed: 11937286]

Palmeri M, Frinkley KD, Zhai L, Gottfried M, Bentley RC, Ludwig K, Nightingale KR. ARFI imaging of the gastrointestinal tract. Ultrasound Imaging. 2005a; 27:75–88.

Palmeri ML, Frinkley KD, Nightingale KR. Experimental studies of the thermal effects associated with radiation force imaging of soft tissue. Ultrasonic Imaging. 2004; 26:100–114. [PubMed: 15344414]

Palmeri ML, Sharma AC, Bouchard RR, Nightingale RW, Nightingale KR. A FEM Model to Simulate Response of Tissue to ARFI Excitation. IEEE Transactions on UFFC. 2005b; 52:1699–1712.

Pislaru C, Kantor B, Kinnick RR, Anderson JL, Aubry MC, Urban MW, Fatemi M, Greenleaf JF. In vivo vibroacoustography of large peripheral arteries. Investigative Radiology. 2008; 43:243–252. [PubMed: 18340248]

Prescott MF, McBride CH, Hasler-Rapacz J, Von Linden J, Rapacz J. Development of complex atherosclerotic lesions in pigs with inherited hyper-LDL cholesterolemia bearing mutant alleles for apolipoprotein B. American Journal of Pathology. 1991; 139:139–147. [PubMed: 1853929]

Prescott MF, Hasler-Rapacz J, von Linden-Reed J, Rapacz J. Familial hypercholesterolemia associated with coronary atherosclerosis in swine bearing different alleles for apolipoprotein B. Annals of the New York Academy of Sciences. 1995; 748:283–292. [PubMed: 7695172]

Pulido M, Angiolillo D, Costa M. Imaging of the Atherosclerotic Plaque. The International Journal of Cardiovascular Imaging. 2004; 10:553–559. [PubMed: 15856642]

Rader DJ, Daugherty A. Translating molecular discoveries into new therapies for atherosclerosis. Nature. 2008; 451:904–913. [PubMed: 18288179]

Raggi P, Taylor A, Fayad Z, O'Leary D, Nissen S, Rader D, Shaw LJ. Atherosclerotic Plaque Imaging – Contemporary Role in Preventive Cardiology. Archives of Internal Medicine. 2005; 165:2345–2353. [PubMed: 16287763]

Rasband, WS. ImageJ. U. S. National Institutes of Health; Bethesda, Maryland, USA: 1997-2007. http://rsb.info.nih.gov/ij/

Rekhter MD. Collagen Synthesis in Atherosclerosis: Too Much and Not Enough. Cardiovascular Research. 1999; 41:376–384. [PubMed: 10341837]

Ribbers H, Lopata R, Holewijn S, Pasterkamp G, Blankensteijn JD, de Korte CL. Noninvasive Two-Dimensional Strain Imaging of Arteries: Validation in Phantoms and Preliminary Experience in Carotid Arteries, in vivo. Ultrasound in Med Biol. 2007; 33:530–540. [PubMed: 17280769]

Rosamond W, Flegal K, Furie K, Go A, Greenlund K, Haase N, Hailpern SM, Ho M, Howard V, Kissela B, Kittner S, Lloyd-Jones D, McDermott M, Meigs J, Moy C, Nichol G, O'Donnell C, Roger V, Sorlie P, Steinberger J, Thom T, Wilson M, Hong Yu. American Heart Association Statistics Committee and Stroke Statistics Subcommittee. Heart Disease and Stroke Statistics—2008 Update: A Report From the American Heart Association Statistics Committee and Stroke Statistics Subcommittee. Circulation. 2008; 117:e25–e146. [PubMed: 18086926]

Rubin, E.; Farber, JL. Pathology. Second Edition. J.B. Lippincott Company; Philadelphia: 1994.

Saijo Y, Jorgensen CS, Falk E. Characterization of Collagen Fibers in Atherosclerotic Plaques in Mice. Acoustical Imaging. 2000; 25:363–368.

Saijo Y, Tanaka A, Iwamoto T, dos Santos Filho E, Yoshizawa M, Hirosaka A, Kijima M, Akino Y, Hanadate Y, Yambe T. Intravascular two-dimensional tissue strain imaging. Ultrasonics. 2006; 44:E147–E151. [PubMed: 16872653]

Sanz J, Fayad ZA. Imaging of atherosclerotic cardiovascular disease. Nature. 2008; 451:953–957. [PubMed: 18288186]

Schuijf J, Poldermans L, Shaw LJ, Jukema JW, Lamb HJ, de Roos A, Wijns W, van der Wall EE, Bax JJ. Diagnostic and Prognostic Value of Non-Invasive Imaging in Known or Suspected Coronary Artery Disease. European J Nucl Med Mol Imaging. 2006; 33:93–104. [PubMed: 16320016]

Shaar JA, van der Steen AFW, Mastik F, Baldewswing RA, Serruys PW. Intravascular Palpography for Vulnerable Plaque Assessment. J of the Am Col Of Cardiology. 2006; 47:C86–91.

Shi Y, Witte R, O'Donnell M. Identification of Vulnerable Atherosclerotic Plaque Using IVUS-Based Thermal Strain Imaging. IEEE Trans Ultrason Ferroelec Freq Control. 2005; 52:844–850.

Soo MS, Ghate SV, Baker JA, Rosen EL, Walsh R, Warwick BN, Ramachandran AR, Nightingale KR. Streaming Detection for Evaluation of Inderterminate Sonographic Breast Masses: A Pilot Study. AJR Women's Imaging. 2006; 186:1335–1341.

Tardif JC. Atherosclerosis imaging. Can J Cardiol. 2005; 21:1035–9. [PubMed: 16234886]

Trahey G, Palmeri M, Bentley R, Nightingale K. Acoustic radiation force impulse imaging of the mechanical properties of arteries. Ultrasound Med Biol. 2004; 30:1163–1171. [PubMed: 15550320]

van der Meer IM, del Sol A Iglesias, Hak AE, Bots ML, Hofman A, Witteman JC. Risk factors for progression of atherosclerosis measured at multiple sites in the arterial tree: the Rotterdam Study. Stroke. 2003; 34:2374–2379. [PubMed: 12947155]

Van Mieghem CA, McFadden EP, de Feyter PJ, Bruining N, Schaar JA, Mollet NR, Cademartiri F, Goedhart D, de Winter S, Granillo GR, Valgimigli M, Mastik F, van der Steen AF, van der Giessen WJ, Sianos G, Backx B, Morel MA, van Es GA, Zalewski A, Serruys PW. Noninvasive detection of subclinical coronary atherosclerosis coupled with assessment of changes in plaque characteristics using novel invasive imaging modalities. J of the Am Col Of Cardiology. 2006; 47:1134–1142.

Viola F, Kramer MD, Lawrence MB, Oberhauser JP, Walker WF. Sonorheometry: a noncontact method for the dynamic assessment of thrombosis. Ann Biomed Eng. 2004; 32:696–705. [PubMed: 15171624]

Wickline SA, Neubauer AM, Winter PM, Caruthers SD, Lanza GM. Molecular Imaging and Therapy of Atherosclerosis with Targeted Nanoparticles. Journal of Magnetic Resonance Imaging. 2007; 25:667–680. [PubMed: 17347992]

Womersley JR. Oscillatory Motion of a Viscous Liquid in a Thin-Walled Elastic Tube - I: The Linear Approximation for Long Waves. Phil. Mag. 1955; 46:199–221.

Yuan C, Kerwin WS, Yarnykh VL, Cai J, Saam T, Chu B, Takaya N, Ferguson MS, Underhill H, Xu D, Liu F, Hatsukami TS. MRI of Atherosclerosis in Clinical Trials. NMR in Biomedicine. 2006; 19:636–654. [PubMed: 16986119]

Zhang XM, Greenleaf JF. Noninvasive generation and measurement of propagating waves in arterial wall. J Acoust Soc Am. 2006; 119:1238–1243. [PubMed: 16521784]

Zhang XM, Greenleaf JF. Estimation of tissue's elasticity with surface wave speed (L). J Acoust Soc Am. 2007; 122:2522–2525. [PubMed: 18189542]

Zheng ZJ, Croft JB, Giles WH, Mensah GA. Sudden cardiac death in the United States, 1989 to 1998. Circulation. 2001; 104:2158–2163. [PubMed: 11684624]

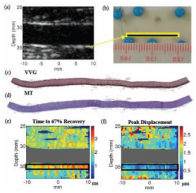

Figure 1.

A B-Mode image of the normal lipid control pig *in vivo* iliac artery is shown in (a); (b) shows an *en face* image of the excised vessel with the yellow rectangle indicating the tissue region that appears as the far arterial wall in B-Mode and ARFI images. Histology matched to the far wall of imaging is shown in (c) (VVG) and (d) (MT), where no atherosclerosis is apparent. Time to recovery from peak ARFI displacement is shown in (e), with color indicating recovery time in ms. A parametric image of peak ARFI induced displacement is shown in (f), with color mapped to displacement in μm. Note the uniform response across the distal vessel wall (black box), which spatially corresponds to sections presented in Fig. (c) & (d). The imaging focal depth was 36 mm. © 2006 IEEE

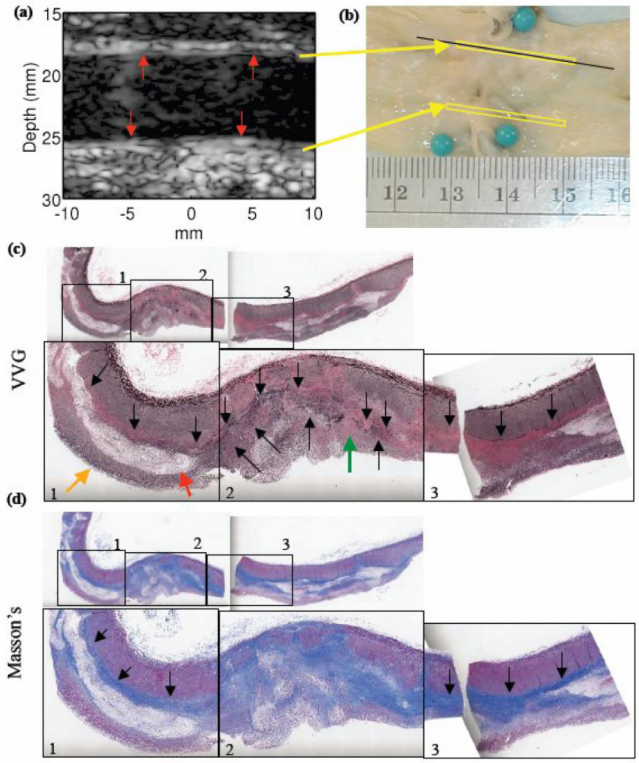

Figure 2.

A matched B-mode image of an *in vivo* left iliac artery is shown in (a). In (b), the en face image of the excised vessel is shown, along with yellow boxes indicating the locations of the near and far walls in B-Mode and ARFI imaging. The black line represents the position of sectioning for histology. Sections stained with VVG (c) and MT (d) for elastin and collagen, respectively, are displayed. Boxes 1, 2, and 3 span the lateral imaging FOV and are shown at higher magnification to highlight immunohistochemical details. Note that these numbered boxes are spatially matched to those of Fig 3(a) and 3(b). Vessel lumen is at the bottom in (c) and (d). © 2006 IEEE

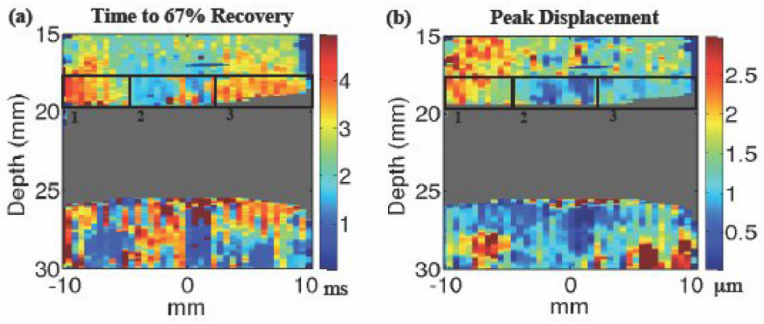

Figure 3.

For the *in vivo* left FH pig iliac artery, time to recovery from peak ARFI displacement is shown in (a), with color indicating recovery time in ms. A parametric image of peak ARFI induced displacement is shown in (b), with color mapped to displacement in µm. Note the variation in response to ARFI excitation across the three labeled boxes, which spatially correspond to the boxes in Fig. 2(c) and 2(d). In regions of higher elastin and collagen content, recovery times are shorter and peak displacements are smaller. ARFI Imaging was performed at a focal depth of 26 mm.

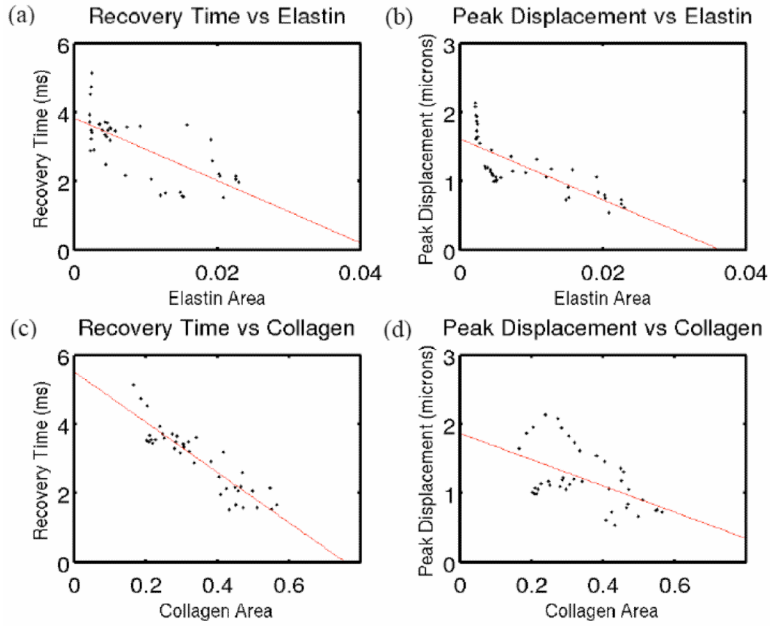

Figure 4.

Scatter plots of median ARFI parameters versus spatially matched elastin and collagen fractional area are shown for the in vivo left FH pig iliac (Figs. 2-3). Median recovery time vs. elastin area is shown in panel a, peak displacement vs. elastin area in panel b, recovery time vs. collagen area in panel c and peak displacement vs. collagen area in panel d. All plots show an inverse relationship between tissue material and ARFI parameter. Least squares linear fits are also superimposed on all scatter plots in red and correlation coefficients are shown in Table 1.

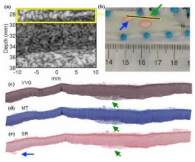

Figure 5.

A B-Mode image of an *in vivo* DH pig iliac artery is shown in panel a; no atherosclerosis is apparent. The *en face* image of the vessel in panel b shows three focal atherosclerotic plaques outlined in red. Yellow rectangles in panels a and b are spatially aligned and indicate the tissue that appears are the near wall in ARFI and B-Mode images. The black line in the *en face* image (panel b) indicates the region of sectioning for matched immunohistochemistry. Three stained sections are shown: VVG (panel c), MT (panel d), and SR (panel e). Green and blue arrows point to two plaques.

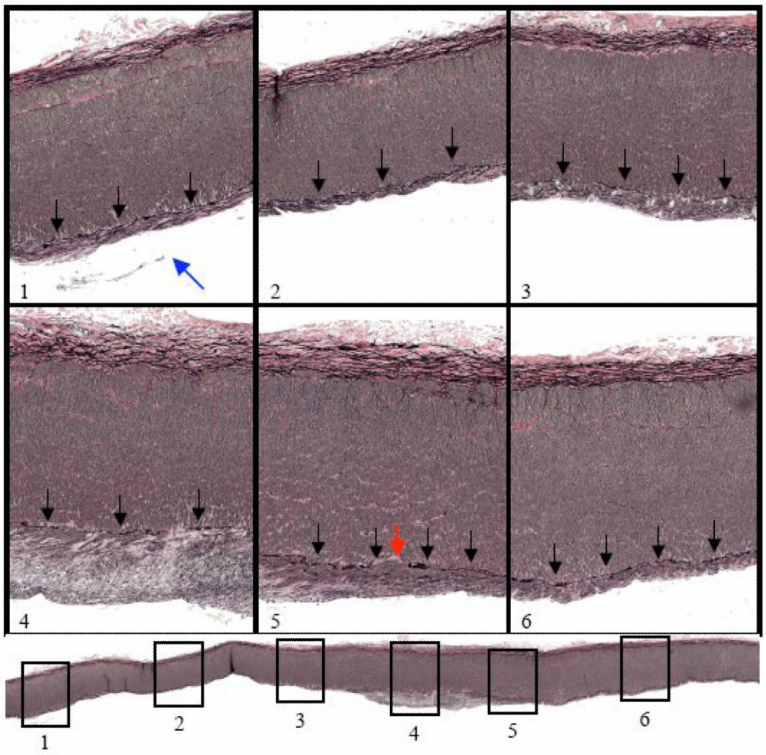

Figure 6.

VVG stain for elastin (black) in a tissue section spatially matched to the ARFI and B-Mode images of Fig. 5. The entire section is shown at bottom. Six regions of the vessel are magnified to illustrate changes in the IEL. In box 1, which includes a small focal plaque (blue arrow), some degradation of the IEL (black arrows) is observed. In box 2 the IEL appears intact with minimal degradation. In box 3, where intimal thickening is more pronounced than in boxes 1 and 2, the IEL appears to have large gaps indicating degradation. This continues into box 4, the thickest part of the second focal atherosclerotic plaque. In box 5, although there are some gaps in the IEL (red arrow), it appears thicker than boxes 1-4 indicating an overall larger elastin content. The IEL in box 6 appears intact and thick as in box 5.

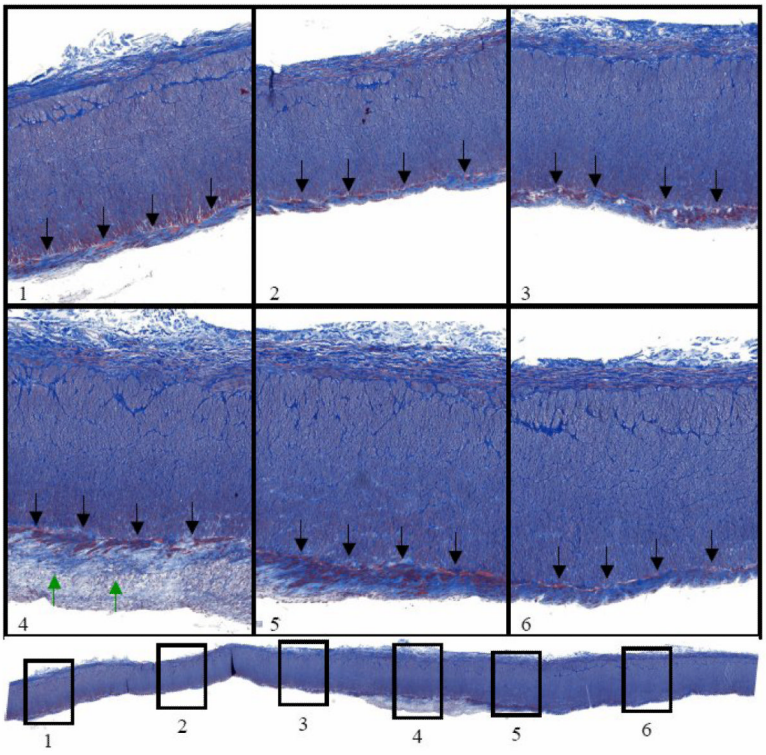

Figure 7.

MT stain indicating collagen (blue) in a tissue section spatially matched to the ARFI and B-Mode images of Fig. 5. The entire section is shown at bottom, with six highlighted regions shown at higher magnification, as in Fig. 6. In boxes 1-3, moderate collagen deposition is seen, with slightly higher collagen deposition in box 3 (black arrows). In box 4, which contains a thick portion of the second focal plaque, extensive collagen deposition is observable, but the collagen is loosely packed, especially nearer to the lumen (green arrows). In box 5, extensive collagen deposition is also apparent; however, the collagen is more densely packed and confined to a smaller area. Box 6 shows only moderate collagen deposition, similar to box 3.

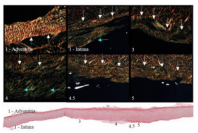

Figure 8.
SR stain under linearly polarized light microscopy for differentiating collagen subtype. Collagen type I fibers, which are generally thicker and stiffer than type III fibers, appear red. Collagen type III fibers appear green. The entire section is shown at bottom with labeled regions of interest. The numbers spatially correspond to the numbered boxes of Figs. 6 and 7. The regions of interest are shown at higher magnification to highlight collagen content (arrows). Notably, while boxes 4, 4.5, and 5 exhibit the highest collagen content in the tissue section, box 4 is primarily comprised of loosely packed type III fibers (blue arrows), while boxes 4.5 and 5 are primarily comprised densely packed type I fibers (white arrows).

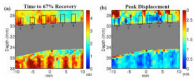

Figure 9.
Parametric time to recovery from peak ARFI induced displacement (a) and ARFI-induced peak displacement (b) images are shown with color indicating recovery time in ms and displacement in μm, respectively. The recovery time image shows slowest recovery exhibited by tissue in boxed regions 1, 3, and 4, where elastin degradation is most severe. The peak displacement image shows the smallest ARFI-induced displacements exhibited by tissue in boxed regions 4 and 5, where collagen deposition is highest. Notice that peak displacements are slightly larger in box 4 than in 5, spatially corresponding to the higher collagen type III content of box 4.

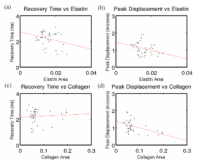

Figure 10.

Scatter plots of median ARFI parameters versus spatially matched elastin and collagen fractional area are shown for the in vivo left DH pig iliac (Figs. 5-9). Panels a, recovery time vs. elastin area, and b, peak displacement vs. elastin area, show an weak inverse relation between elastin and ARFI parameter. Panel c shows no relation between recovery time and collagen, a relationship not expected to be strong. Peak displacement vs. collagen is shown in panel d with an inverse relationship. Least squares linear fits are also superimposed on all scatter plots in red with respective correlation coefficients shown in table 1.

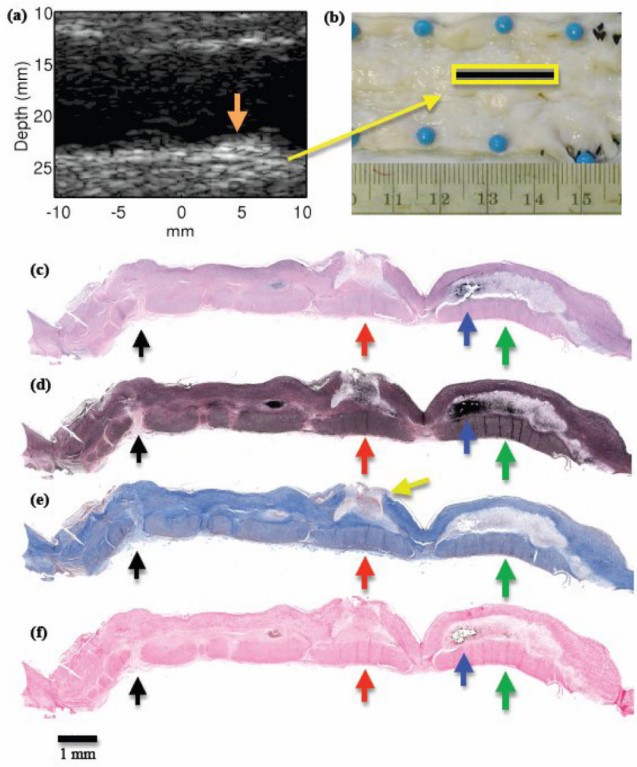

Figure 11.

A matched B-Mode of an *in vivo* FH artery is shown (a), with an *en face* image showing diffuse atherosclerosis (b). While the pervasiveness of atherosclerosis is not readily apparent in the B-Mode (a), what appears to be a small lesion is seen to protrude into the lumen (orange arrow). In histology stains, H&E (c), VVG (d) and MT (e), two atheromatous plaques are visible. One has a thick, intact fibrous cap (green arrows) and the other a disrupted fibrous cap (red and blue arrows). A disruption in the IEL is also noted (black arrows). Alizarin Red stain (panel f) confirms calcium deposition in the right atheromatous plaque (yellow arrows).

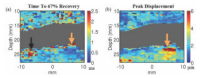

Figure 12.
Parametric ARFI images matched to the B-Mode in 11 (a) are shown. In the recovery time image (a) faster recovery is observed in the region of the intact fibrous cap (orange arrow). Slower recovery is observed in the location of IEL disruption (black arrow). In the image of peak displacement (b), a region of large displacement that is covered by tissue exhibiting smaller displacement is observed in position of the right atheromatous plaque (orange arrow).

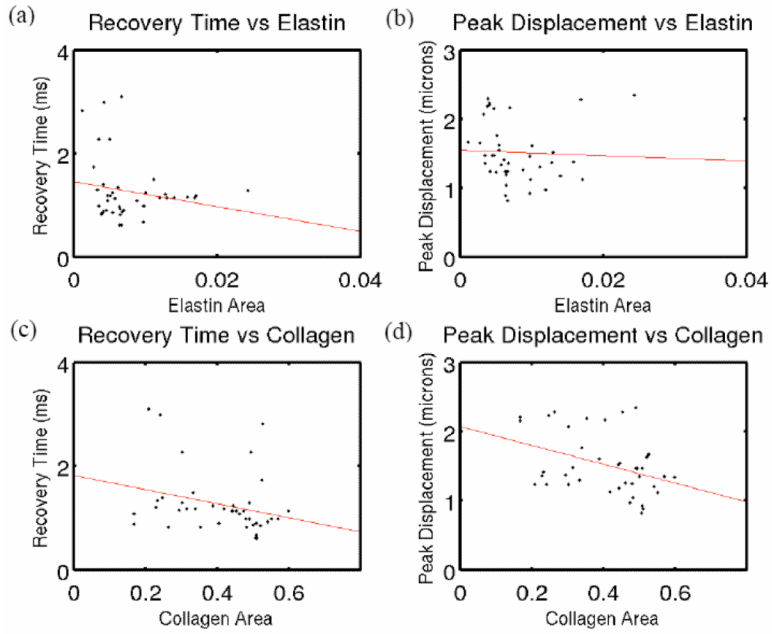

Figure 13.

Scatter plots of median ARFI parameters versus spatially matched elastin and collagen fractional area are shown for the in vivo left FH pig iliac 2 (Figs. 11-12). Areas of calcium indicated in staining (Fig. 11 panel d) were excluded from analysis. Median recovery time vs. elastin area is shown in panel a, peak displacement vs. elastin area in panel b, recovery time vs. collagen area in panel c and peak displacement vs. collagen area in panel d. Only panel d, peak displacement vs. collagen area shows a statistically relevant inverse correlation. Least squares linear fits are also superimposed on plots in red.

Ultrasound Med Biol. Author manuscript; available in PMC 2011 June 1.

Table 1

Correlation coefficient values (Rho) and P-values are shown for all 4 possible relations between ARFI parameter (recovery time or peak displacement) and spatially matched tissue material (elastin or collagen) in each diseased example presented.

	***In vivo Left* FH**		***In vivo* Left DH**		**In vivo Left FH 2**	
	Rho	**P-value**	**Rho**	**P-Value**	**Rho**	**P-Value**
Recovery Time &. Elastin	−0.7015	2.740e-07	−0.2732	0.0840	−0.1921	0.2288
Peak Displacement & Elastin	−0.7595	8.532e-09	−0.3143	0.0454	−0.0426	0.7814
Recovery Time & Collagen	−0.9051	4.602e-16	0.0758	0.6375	−0.2764	0.0802
Peak Displacement & Collagen	−0.5226	4.560e-04	−0.5047	0.0008	−0.3834	0.0134